Research Square

Preprints are preliminary reports that have not undergone peer review.
They should not be considered conclusive, used to inform clinical practice,
or referenced by the media as validated information.

Advanced EVS Pixel Modeling to Improve Dim RSO Detection up to 2.9× and Enable Accurate Photometric Reconstruction for SDA

Brian McReynolds

brian.mcreynolds@afacademy.af.edu

United States Air Force Academy

Rachel Oliver

Air Force Institute of Technology

Zachry Theis

Air Force Research Laboratory

Peter McMahon-Crabtree

Air Force Research Laboratory

Michal Zolnowski

6 ROADS

Tobi Delbruck

Institute of Neuroinformatics

Research Article

Keywords: Event-based Vision, Space Domain Awareness, Sensor Optimization, Photometric Reconstruction

Posted Date: April 16th, 2026

DOI: https://doi.org/10.21203/rs.3.rs-8900804/v1

License: This work is licensed under a Creative Commons Attribution 4.0 International License.
Read Full License

Additional Declarations: No competing interests reported.

Version of Record: A version of this preprint was published at The Journal of the Astronautical Sciences on July 28th, 2026. See the published version at https://doi.org/10.1007/s40295-026-00610-1.

Advanced EVS Pixel Modeling to Improve Dim RSO Detection up to 2.9× and Enable Accurate Photometric Reconstruction for SDA

Brian McReynolds[1*], Rachel Oliver[2], Zachry Theis[3], Peter McMahon-Crabtree[3], Michal Zolnowski[4], Tobi Delbruck[5]

[1*]Department of Physics and Meteorology, USAF Academy, 2345 Fairchild Dr, USAF Academy, 80840, CO, USA.
[2]Department of Aeronautics and Astronautics, Air Force Institute of Technology, 2950 Hobson Way, Wright-Patterson AFB, 45433, OH, USA.
[3]Space Vehicles Directorate, Air Force Research Laboratory, 3550 Aberdeen Ave SE, Kirtland AFB, 87117, NM, USA.
[4]6Roads, Space Surveillance and Tracking Services, 55A Godebskiego Street, 31-999, Krakow, Poland.
[5]Institute of Neuroinformatics, University of Zurich and ETH Zurich, Winterthurerstrasse 190, 8057, Zurich, Switzerland.

*Corresponding author(s). E-mail(s): brian.mcreynolds@afacademy.af.edu;
Contributing authors: rachel.oliver.2@spaceforce.mil; zachry.theis.1@spaceforce.mil; peter.mcmahon-crabtree@spaceforce.mil; michal.zolnowski@6roads.com.pl; tobi@ini.uzh.ch;

Abstract

Event-based Vision Sensors (EVS) have been increasingly utilized for Space Domain Awareness (SDA) applications over the past several years. Newer models demonstrate improved performance compared to early generation systems; however, the absolute limits of their sensitivity with respect to fundamental physical parameters (i.e. on-chip photon flux) for detecting dim point source objects has not been fully quantified. Additionally, the complex exercise of optimizing

tunable sensor biases for SDA has not been explored for the newest generation sensors. This work shows that with optimized biasing, scan rate, and a novel denoising strategy, the IMX636 sensor is capable of detecting point sources that produce on the order of several hundred photons per second on the focal plane. Our detailed characterization allows users of the technology to predict detection limits when paired with varied optical systems. The result is included in an open-source software tool. Additionally, bias optimization is shown to extend sensitivity by 1.05 visual magnitudes, m_v, and when coupled with the our denoising method, enables detection of $\mathbf{2.9}\times$ more star streaks compared with default biases. The detailed modeling of pixel level performance further enables a method for reconstructing object brightness from event camera output by calibrating the sensor's dark current and incorporating a model that accounts for the pixel's illumination dependent temporal response and logarithmic compression. Ultimately, the ability to accurately extract photometric information from an event camera can extend to other characterization methods including polarimetry and spectral analysis with proven EVS benefits of excellent temporal resolution, low power, sparse data output.

Keywords: Event-based Vision, Space Domain Awareness, Sensor Optimization, Photometric Reconstruction

1 Introduction

Neuromorphic, Event-based Vision Sensors (EVS) have a unique, frame-free operating paradigm and offer significant benefits over conventional, frame-based sensors [5]. As a result, EVS have garnered recent interest for space sensing tasks due to performance advantages like high temporal resolution, wide-dynamic range, and data sparsity resulting from their frame-free sensing paradigm [1]. Several studies showcase their capabilities for detecting Resident Space Objects (RSO)s, but only three have reported empirical measurements of limiting performance [19, 10, 18]. Early studies concluded that second and third generation EVS lag state-of-the-art, scientific CMOS cameras in absolute sensitivity but offer significant advantages in temporal resolution and data sparsity [10], whereas the current 4th generation cameras made significant improvements in low light performance and sensitivity. However, performance limits have only been reported for a specific combination of sensor and optic, so they do

not directly translate to fundamental performance limits and are not useful for predicting sensor capabilities when paired with varied optical systems. Additionally, no previous studies explored the vast parameter space of user-defined sensor biases available in EVS. To establish the true limits of EVS performance, we consider pixel-level circuit operation to apply novel techniques for managing EVS noise to optimize sensitivity and improve dim, sub-pixel, point source object detection. Using a custom-built, photometrically-calibrated RSO simulator, we explore the many degrees of freedom offered by adjustable camera biases and report results from the most advanced commercially available EVS, the Sony/Prophesee IMX636. Finally, we demonstrate a novel denoising method to offset the excess noise introduced by increasing camera sensitivity. We show that just a small fraction ($\sim$2%) of pixels tend to dominate the background noise (>99% background events). Additionally, we demonstrate that each pixel's average noise rate remains relatively constant in time, allowing us to apply a computationally efficient background subtraction method.

This paper highlights several key results. Foremost, our optimized biases increase sensitivity by up to 1.05 visual magnitudes (2.6x) compared to stock biases which have been used predominantly in EVS SDA efforts to date. Our detailed characterization methodology demonstrates that, when optimally biased, modern EVS are capable of detecting point source objects producing as few as 1.3k photons per second with transit speeds of 6.8 pix/sec on the sensor's focal plane. Further after fitting a model that accounts for the pixel's finite temporal response near the dark current limit, our results suggest that for transit speeds on the order of 1 pixel/second, the sensitivity limit can be decreased to approximately 450 photons/second. These characterization results are captured in an open-source software model allowing potential EVS users to predict sensor response as a function of object brightness (visual magnitude), optical system (focal length, f/#, point spread function) and object/scan speeds. Combining bias optimization and noise reduction during an on-sky collection, we demonstrate

the ability to detect 2.9x more star streaks compared to stock biases with an effective data rate of less than 0.02 events/pixel/second.

We extend the results of our pixel level characterization and modeling to reconstruct photometric information from EVS output. Simply detecting RSOs and estimating their trajectories is foundational but not the only goal in SDA. The ability to extract absolute photometric information would expand potential EVS utility under the SDA umbrella. Ralph et al. discussed the practicality of extracting photometric information from EVS output and proposed that relationships between the event density (events per second per pixel) and equivalent diameter of a celestial object can be leveraged to estimate brightness variations [18]. The ability to detect brightness variations at high speeds could also be advantageous for applications such as light-curve-inversion [4]. Characterizing RSO using photometric, polarimetric, or spectral measurements is another important task for SDA systems to assist in identification of new or previously unknown objects.

Recently, a few groups have demonstrated the ability to map EVS output to object brightness with limited success, but the estimation error increases dramatically for dimmer objects. Using a custom point source RSO simulator to simulate sub-pixel, point source objects moving against a dark background and recording with a 4th generation Sony IMX636 sensor, we show that EVS response can be reliably mapped to object brightness. We first develop a theoretical model from first principles using both the logarithmic compression and the illumination dependent, finite temporal response bandwidth of the pixel's photoreceptor. Incorporating the pixel's temporal response facilitates accurate photometric reconstruction even at the lowest detectable light levels. Ultimately, this new ability to extract photometric information from an EVS event stream expands potential use cases of EVS for SDA, providing a future pathway for data efficient photometric, spectral, and polarimetric RSO characterization with high temporal resolution.

2 EVS Description

2.1 Basic Operation

Figure 1 depicts the basic, three-stage pixel architecture that enables event-based change detection exploited in EVS pixels. The photoreceptor compresses photocurrent logarithmically to output voltage V_{p}. A source-follower buffer filters V_{p} prior to the change amplifier, which effectively amplifies changes around a fixed reference by the well-matched capacitor ratio $\frac{C_1}{C_2}$. Two comparators continuously monitor the output signal V_{diff}, and generate a binary output if it increases (ON) or decreases (OFF) by predetermined contrast threshold values, θ_{ON} or θ_{OFF}, compared to the previously "memorized" reference level. These binary output "events" are read off-chip by peripheral circuits and packaged into Address Event Representation (AER) output which consists of a μs timestamp, t, ON or OFF polarity, p, and the pixel's (x,y) address on the focal plane. After each event is read-out, the pixel waits a tunable refractory period before resetting the reference to track subsequent changes to the photocurrent.

Figure 2 illustrates event-generation in response to a time varying input signal. In the top plot, V_{p} represents the log-photocurrent. The bottom plot represents the change amplifier output. Initially, the reference level corresponds to the instantaneous value of the log-photocurrent. As V_{p} increases, the input signal is inverted and amplified in the second stage. Once the inverted change amplifier output decreases by one threshold below the reset level, an ON event is generated, indicating that the photocurrent has increased since the previous reset. The change amplifier output is immediately reset, and after the refractory period, again begins to track changes in the input signal. In the example shown, the gradual rise and fall of the input signal generates three ON events followed by three OFF events.

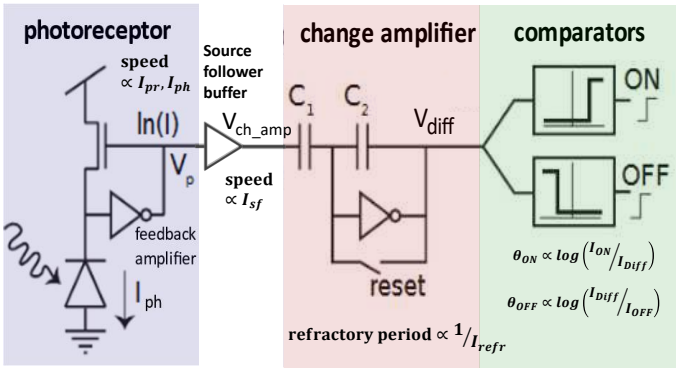


Fig. 1 Abstract EVS pixel architecture, adapted from [8].

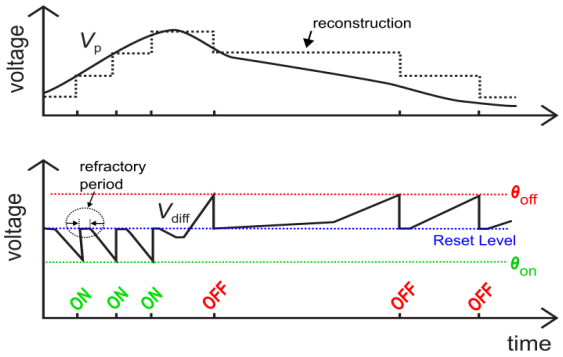


Fig. 2 Simple depiction of EVS pixel operation [8].

2.2 Bias Description

As part of this study, we examine various bias combinations to find an optimal setting for SDA applications. EVS have a number of tunable bias parameters that directly impact sensor performance. These are typically referred to as bias currents and the most critical are listed in Figure 1 as I_{xx} where xx is a description of the corresponding circuit element. The most important performance parameters for EVS are the threshold levels, which define the amount of signal change necessary to generate an event. Because EVS report both positive (ON) and negative (OFF) signal changes, both thresholds are set independently and can be individually tuned. Three bias currents determine the threshold levels. Their names differ slightly between camera models,

but typically, the ON threshold, θ_{ON} is proportional to log of the bias current ratio $I_{\mathrm{ON}}/I_{\mathrm{diff}}$ and the OFF threshold is proportional to the log of the ratio $I_{\mathrm{diff}}/I_{\mathrm{ON}}$.

The other important bias parameters that influence sensor behavior are related to the temporal response of each pixel. I_{sf} (I_{fo} in the IMX636 sensor) tunes the Low-Pass Filter (LPF) corner frequency of the source follower buffer. A higher value increases the corner frequency, allowing the pixel to detect signals that change more rapidly, but also allowing higher frequency noise components into downstream circuit elements. I_{refr} adjusts the refractory period, or "dead-time" between consecutive events. Increasing this period can also have important implications in reducing noise rates [12], but also can lead to signal loss when recording very large, fast signal changes [15]. The IMX636 sensor used in this study also includes a high-pass filter option (not shown in Fig. 1) to prevent the sensor from responding to low frequency changes or slowly drifting signals.

2.3 SDA Specific Considerations

A significant goal of this study is to establish baseline performance of the IMX636 for SDA applications and push the limits of the technology by optimizing sensitivity to detect the dimmest possible point source objects against a dark background. When operating EVS in the context of SDA, it is important to consider a few key performance characteristics based on physical limitations of the pixel circuit itself. First, EVS have historically been limited by noise, which manifests as "events" that are recorded by the sensor in the absence of any true signal change. Noise rates vary with background illumination, and for prior generation EVS, noise performance in the dark was a significant hindrance to SDA. And second, despite being known for high temporal resolution, EVS temporal response is reduced when the photocurrent is low.

Noise presents a significant issue as high noise rates can make it impossible to distinguish true signal events. Furthermore, high noise rates also somewhat negate the data-sparsity of EVS output, which is a significant performance advantage over

conventional frame-based imagers in many applications including SDA. Noise can be managed to some extent with biases, but not without important tradeoffs. Reducing the source follower bias shifts the LPF corner frequency lower and removes higher frequency noise components, but also reduces the ability to detect fast signals. Increasing the high-pass corner frequency reduces low frequency noise components, but will prevent the pixel from responding to slower moving signals. Increasing threshold levels also limits noise by reducing the likelihood that shot noise will generate enough signal change to trigger an event, but at the cost of sensitivity. One previous study showed that applying imbalanced thresholds in favor of more ON events can reduce noise with increased ON sensitivity [12], which was shown to be an effective bias technique for SDA [13].

Fast temporal response and high temporal resolution despite low data rates are hallmarks of EVS sensors, but these benefits can be greatly reduced in the dark. The logarithmic amplifier in the photoreceptor used in EVS pixels acts as a second-order LPF [2]. Under low illumination, the dominant pole of the transfer function is determined by and scales monotonically with the photocurrent [6, 7]. As a result, the pixel's temporal response near the dark current limit is several orders of magnitude slower than when the background photocurrent is high (for example, in daylight conditions). The background during night-time SDA collects is typically well below the dark current limit of EVS pixels, and for the DAVIS346 sensor, was shown to be on the order of a few Hz [13] near this limit. The bias configurations tested during this study were customized to explore both the sensitivity and temporal response limits of the IMX636 EVS with realistic limits on acceptable noise rates.

3 Methodology

A custom, moving point source generator was developed to study the performance limits of EVS cameras for detecting moving, sub-pixel objects against a dark background. This allowed multiple bias configurations to be tested with identical stimuli. The position of each point source was calibrated in order to reliably map true signal events in the sensor output and accurately remove noise, which allowed us to test more sensitive (noisier) bias combinations. Source brightness was carefully calibrated in order to extract fundamental physical limits and define sensitivity of the IMX636 sensor in terms of minimum on-chip photon flux. Observing sensor response to point sources of varying brightness and speeds allowed us to parameterize a model of the pixel response and develop an open source Graphical User Interface (GUI) for predicting EVS output for a range of objects of differing speed and brightness with various optical system parameters and biases. Finally, the best-performing bias configuration was applied during an on-sky collection and compared to default, stock biases.

3.1 Lab Set-up

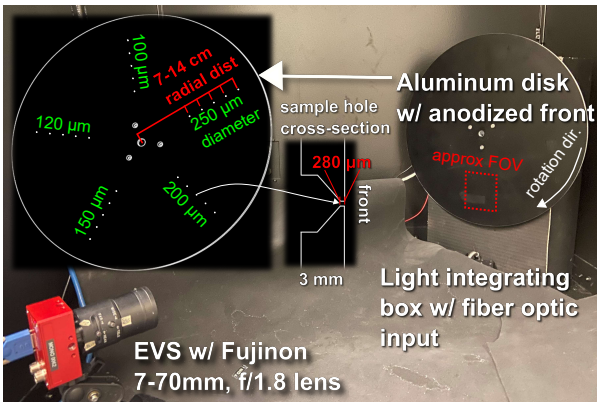


Fig. 3 Disk and lab set-up

The lab setup used in this study was detailed in [13] and is depicted in Fig. 3. The main component of the point source simulator is a custom-fabricated, anodized aluminum disk with precision drilled holes of 100-250 μm diameter located at radial distances between 7-14 cm from center. The backside of each hole was drilled out as shown in the inset to reduce back-scattering and reflection as the light from the integrating box propagates through the openings. Moving point source targets are simulated by rotating the disk in front of an 'integrating' light box with variable input intensity and viewed by the IMX636 EVS through a 7-70mm, F/1.8 lens. A high-power, white LED was used to illuminate the integrating "box" and light intensity was controlled by the circuit described in [16]. The speed of the disk was controlled by a programmable motor manufactured by Henschel Robotics [1]. The entire assembly was placed into a dark box to approximate night sky illumination, which for typical viewing conditions is well below the dark current limit of the photodiode at $\approx$ 1 mlux.

3.2 Photometric Calibration

Point source brighness was calibrated over the range of possible input voltages. A Tektronix J17 photometer was used with the J1811 illuminance head to calibrate the illuminance $E_{\mathrm{v,source}}$ in lux at the light source output as a function of power supply voltage. Using the DAVIS346 Active Pixel Sensor (APS) functionality, we determined that 90% of the illuminance at the light source output was able to exit through each drilled hole, meaning only about 10% of the light energy was lost to reflection within the hole cavity. Luminous flux for each point source ϕ_{v} was then calculated as

$$\phi_{\mathrm{v}} = 0.9\, E_{\mathrm{v,source}} \pi r_{\mathrm{hole}}^2 \tag{1}$$

where r_{hole} is the radius of each opening and 0.9 is the scaling term accounting for loss within the hole cavity. For each opening, luminous flux is then converted to apparent

[1] Henschel Robotics GmbH

illuminance at the entrance pupil of the optic using the relationship

$$E_{\mathrm{v,pupil}} = \frac{\phi_{\mathrm{v}}}{\pi d^2}, \tag{2}$$

where d is the distance from the disk to the entrance pupil of the camera. The factor of πd^2 in the denominator is obtained by treating each opening as a uniform disk, integrating the total illuminance (including the $\cos\theta$ dependency) over a hemisphere with radius d and setting it equal to the luminous flux at the hole opening. The full derivation is included in [11]. Once obtained, $E_{\mathrm{v,pupil}}$ can be converted to an on-chip photon rate, R_{ph}, by

$$R_{\mathrm{ph}} = E_{\mathrm{v,pupil}}\pi\left(\frac{D}{2}\right)^2 \times 1.12 \times 10^{16}, \tag{3}$$

where D is the diameter of the aperture or entrance pupil and 1.12×10^{16} is the scalar conversion between lm and photons/sec in the visible band for white light estimated by [17]. Assuming point sources can be focused onto a single pixel, R_{ph} is a practical metric for EVS sensitivity to dim-point source objects as it is indifferent to the optical system being used, unlike visual magnitude.

3.3 Spatial Calibration

In order to reliably identify true signal in the presence of a noisy background, the (x,y) position of each point source on the focal plane was calibrated to the instantaneous position of the disk motor as depicted in Fig. 4. Point source position ground truth was constructed by creating pixel maps of maximum event counts recorded in response to the highest source voltage (i.e. point source brightness) for each set of holes as the disk rotated, creating streaks across the focal plane. Using a low-noise bias configuration, the maximum event count along each streak was extracted as ground truth for the

position of each point source as a function of motor angular position. The disk and camera were both controlled by a Jupyter notebook which allowed synchronization of each recording to a specific starting and stopping angle of the motor. This was used to correlate the motor's exact angular position corresponding to the each target's transit of each pixel along the streaks. In subsequent recordings, the motor's angular position was linearly interpolated to extract only events with timestamps correlating to an actual target, providing reliable ground truth to analyze sensor response as a function of either point source brightness or speed.

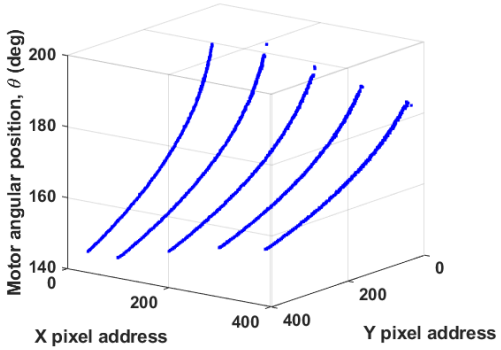


Fig. 4 Target map relating motor position to x,y address on the focal plane to provide target position ground truth and facilitate noise removal when evaluating more sensitive and noisier bias configurations.

3.4 Bias Selection

Table 1 describes the seven bias configurations selected for analysis in this study. The first, IMX-1, is the standard bias configuration that is loaded by default when the sensor is run with the open source MetaVision software provided by Prophesee. Each number represents a deviation from the default bias setting, with zero being the default. A lower number corresponds to a lower bias current, with the exception of I_{off}, where the lower number results in a more sensitive OFF threshold. All configurations but IMX-1 and IMX-2 employ the strategy of setting a more sensitive ON threshold

Bias	I_{fo}	I_{hpf}	I_{refr}	I_{on}	I_{off}	I_{diff}
IMX-1	0	0	0	0	0	0
IMX-2	0	0	0	-46	-25	0
IMX-3	55	0	0	-44	0	0
IMX-4	0	0	0	-47	0	0
IMX-5	-35	0	0	-48	0	0
IMX-6	-35	0	-20	-62	0	0
IMX-7	-35	60	-20	-62	0	0

Table 1 Bias configurations evaluated.

level as demonstrated to be the most effective method for tuning the DAVIS346 EVS in [13]. Default biases resulted in the lowest noise rate of ≈ 0.03 events per second per pixel (ev/s/px). All other bias configurations were fine-tuned to result in background noise rates of ≈ 1 ev/s/px, and each employs a different combination of biasing strategies intended to optimize signal to noise.

4 Sensitivity and Modeling

4.1 Sensitivity

Each of the seven bias configurations shown in Table 1 was tested in order to empirically determine the best performing bias for detecting dim point source objects. The motor was run near its minimum speed setting to reduce the effects of the LPF properties of the photoreceptor circuit under dim lighting conditions, resulting in a transit speed of ≈ 6.8 pixels per second (px/s) on the focal plane. For each, bias configuration, data was recorded for calibrated brightness levels ranging from $\approx 2k$ to $\approx 200k$ photons/sec (ph/s), and matched events correlating to mapped ground truth were extracted using the motor's instantaneous angular position, the timestamp of each event, and the target mapping described in Sec. 7.

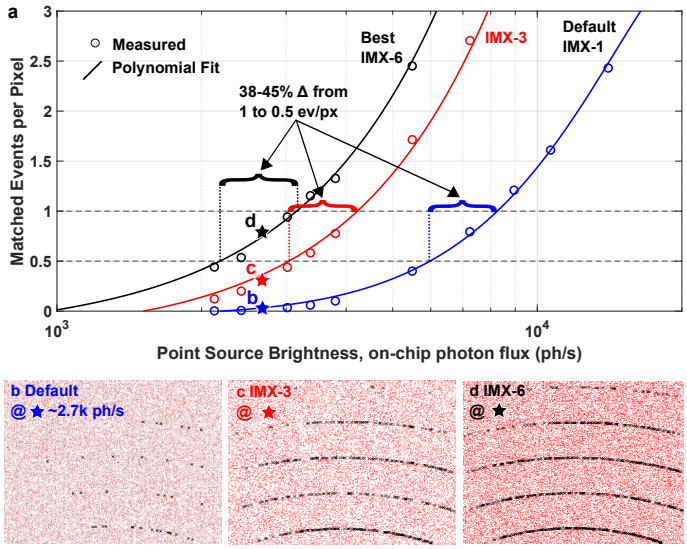


Fig. 5 Sensitivity comparison for three different bias configurations

Figure 5 **a** plots results for three of the selected bias configurations, and part **b** shows the mapped ground truth events (black x's) against the noise event density (red dots) for each of the configurations plotted in part **a** for a point source brightness of 2.7k ph/s. A third-order polynomial was found to fit the raw data over the range displayed in Fig. 5 and used to interpolate the object brightness corresponding to a particular response probability (matched events per pixel). We assume that a minimum of 50% of the pixels along a streak must respond in order for a streak to be reliably detected, so we choose the 0.5 matched events per pixel intercept to define the minimum detectable on-chip photon rate. Using this criteria, the best performing bias configuration is capable of detecting objects generating as few as 2.3k ph/s, achieving 2.6× better sensitivity than default biases, or using visual magnitude units, an improvement of $2.5\log_{10}(2.6) = 1.05m_{\mathrm{v}}$. For all biases, the increase in object brightness needed to achieve 100% response probability (i.e. 1 matched events per pixel) compared to 50% response probability (0.5 matched events per pixel) is roughly 40%. From part **b**, we can see that the more sensitive bias configuration also results in increased background noise, which we address in Sec. 6. Additionally, it is clear

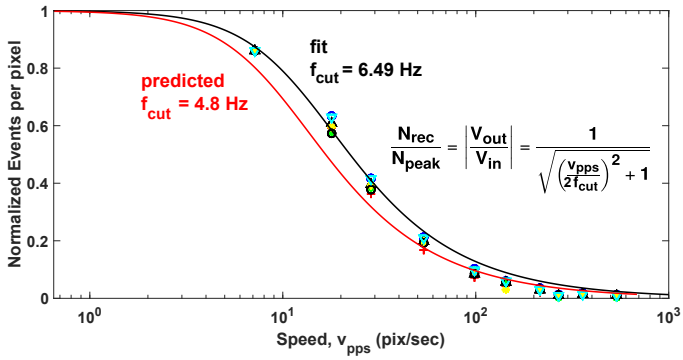


Fig. 6 Normalized events per pixel vs. object speed for a constant brightness point sources. Normalizing the response collapses the number of events per pixel onto the same curve and approximates a 1st-order LPF magnitude response.

that the outer streaks, which are moving 2× faster than the inner streaks generate fewer signal events, indicating that signal attenuation due to the LPF properties of the photoreceptor may in fact be limiting the response.

4.2 Drop in sensitivity with Speed

To analyze the temporal response of the pixel, we conducted a similar analysis as described in Sec. 4.1. We selected a bright, constant point source brightness level of $128k$ ph/s and used different transit speeds to analyze the drop in sensitivity with speed for each bias configuration. Based on the sensitivity results shown in Fig. 5, it is evident that different biases will produce drastically different event counts for the same point source brightness, so the results were normalized to the maximum event count observed at the slowest speed.

Figure 6 portrays the surprising result that the temporal response of the IMX636 is not affected by the bias configuration. Moreover, the corner frequency is much lower than expected based on claims that EVS offer high temporal resolution. Normalized data points for all seven bias configurations (depicted by different markers) were used to fit a first-order LPF transfer function using least squares regression and solve for the cutoff frequency f_{cut}, resulting in an estimate of $6.49Hz$. Despite this surprising

result, combining reported performance metrics for measured response latency and low light cutoff values for a similar EVS model at low illumination, we obtain a prediction of $f_{\text{cut}} = 4.8Hz$ corresponding to an on-chip photon rate of $128k$ph/s (see [11] 5.5.6). The factor of 2 that appears in the fit model accounts for the fact that the size of the generated point sources on the focal plane is roughly the size of one pixel, meaning that as the object transits a single pixel, it generates a current pulse (in time) that is roughly $2\times$ the width of the positive lobe of a sine wave pulse, which is the waveform assumed when using the LPF transfer function shown. The result shown in Fig. 6 has important implications for how EVS should be employed in real world SDA applications. To maximize sensitivity, this suggests the optical system should be designed to limit speed of the point sources to no more than a few pixels per second. In reality, because the corner frequency scales proportionally with photocurrent in very dark conditions, the ability to detect the dimmest point sources will be optimized at even lower speeds. In the Sec. 4.3, we use the results of our measurements and knowledge of EVS characteristics to fit a model that predicts key performance parameters, and in Sec. 4.4 we show how our fit parameters are consistent with a prior report of IMX636 sensitivity with a specific optical setup.

4.3 Model Parameters

Recently, efforts have been made to map EVS output to object brightness with limited success. Figure 7 demonstrates a model that fits our empirical EVS response obtained in Sec. 4.1 for object transit speeds of ≈ 6.8 pix/sec. From Sec. 4.2, we saw that objects producing $128k$ph/s on the focal plane resulted in a corner frequency of $\approx 6.5Hz$. This photon rate produces $\approx 128k\text{ph/s} \times\eta \times e^{-} = 13.3fA$ of photocurrent, assuming the quantum efficiency $\eta = 0.65$, however, based on Low Light Cutoff (LLCO) estimates from Prophesee [3], this is roughly $10x$ the dark current limit of the IMX636 pixel. Because the corner frequency scales proportionally with photocurrent, this implies

that as the point source transits a pixel, the 6.8 pix/sec speed used in our recordings produces a response that is much faster than the dark current corner frequency f_{dark} and the signal would be attenuated significantly for dimmer objects. The fact that the pixel's corner frequency scales proportionally with photocurrent also suggests that the pixel's temporal response will increase when responding to objects of different brightness levels.

Figure 7 demonstrates how accounting for the intensity-dependent LPF characteristics of theEVS pixel facilitates an accurate model of the measured response. A simple model (outlined in black) predicts the expected number of ON events N_{ON} that should be recorded as the object transits a pixel assuming an infinitely fast temporal response. The term ΔI is defined in this case as $\frac{I_{\text{ph}}+I_{\text{dark}}}{I_{\text{dark}}}$, where I_{dark} is the photodiode's dark current and I_{ph} is the photocurrent generated by the object itself. Assuming the refractory period is much faster than the signal change (typically $\approx 100\mu s$), the number of ON events N_{ON} is therefore the number of times the log signal change $log(\Delta I)$ crosses the on threshold θ_{ON}. This simple model depicted by the black dashed line fits the measured data points between 10^4 and 10^5 ph/s, but diverges for very dim and very bright data points. The revised fit model shown in blue accounts for the intensity dependent LPF and is able to accurately map sensor response to object brightness. The signal is attenuated by a first-order LPF transfer function, and the combined terms $f_{\text{dark}}\Delta I$ effectively scale the corner frequency as a function of photocurrent. N_{offset} accounts for the fact that imbalanced ON and OFF thresholds were used, meaning that each pixel's reference level is offset from the mean value of the dark current by some factor of the ON threshold. It is subtracted because it represents the small number of ON events that are "missed" because noise has shifted the pixel reference current slightly above the dark current level.

The blue curve was obtained by using a least-squares regression to fit the final model to the measured data points. Comparing the simple model to our revised model

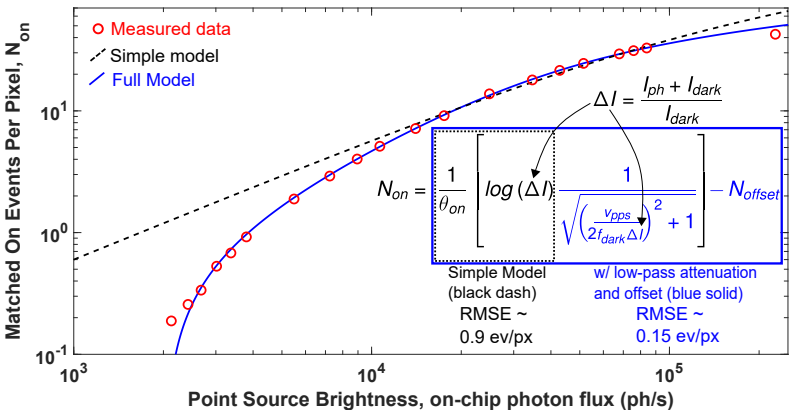


Fig. 7 Matched ON events per pixel vs. object brightness. The simple model (black dashed curve) cannot adequately reconstruct photometric information from EVS events (red circles) when the brightness is very low. The corrected model (solid blue curve) accounts for the intensity dependent LPF and the offset in reset level due to imbalanced ON/OFF thresholds, achieving a RMSE of 0.15, or 6× better than the simple model.

that includes intensity dependent LPF attenuation and N_{offset}, we see that the Root Mean Square Error (RMSE) is reduces from 0.9 ev/px to 0.15 ev/px. Across all seven bias configurations evaluated, fit parameter estimates for non-bias dependent terms were $I_{\text{dark}} = 1.1 \pm 0.5\text{fA}$, $f_{\text{dark}} = 0.55 \pm 0.2$ Hz. The close agreement across all bias configurations provides confidence in using the fit parameters. In addition, the dark current estimate is in close agreement with previous estimates obtained by other means [11]. As expected, parameters that should vary with biases were found to range between $0.05 < \theta_{\text{on}} < 0.15$ and $0.74 < N_{\text{offset}} < 1.02$ across the seven configurations.

4.4 Comparison to Previous Studies

Only three previous studies have attempted to quantify EVS sensitivity for SDA, and only one used the latest generation IMX636 prototype used in this study. All previous studies reported sensitivity in terms of limiting visual magnitude, which makes direct comparisons difficult without correcting for the optical system parameters. Additionally, none specifically addressed how the scan rate or speed of objects being recorded influences sensitivity; however, [10] qualitatively noted a drop in sensitivity

with increased scan rates. Table 2 incorporates empirical estimates of limiting visual magnitude reported in [19, 10, 18]. Using reported optical system parameters, scan rates are converted to pixels per second (px/s) and limiting magnitude is converted to an on-chip photon rate R_{ph}.

Based on the results, it is clear that the 4th generation IMX636 achieves significantly better sensitivity compared to the other two models tested by Zolnowski et al. and McMahon-Crabtree and Monet. Ralph et al. reported a limiting magnitude of 14.45 using a 600mm, $f/3$ optic, resulting in a limiting R_{ph} of $1.24k$ph/s. They also report using default biases, which leads to an apparent discrepancy in the results we obtained with our lab measurements which indicated a limit of $6k$ph/s with default biases. However, upon further investigation, this discrepancy is explained by the temporal response of the sensor. The estimate of $1.24k$ph/s was obtained with a scan rate of just 0.95 px/s, whereas our measurements were taken at a speed of 6.8px/s. Using our f_{dark} estimate of $0.55Hz$ from Sec. 4.3 above, we can reconcile this significant difference in minimum detectable photon rate. Using an order-of-merit estimate, the degree of signal attenuation predicted by the mathematical model shown in Fig. 7 near the dark current limit is $\frac{1}{\sqrt{\left(\frac{0.95}{1.1}\right)^2+1}} \approx 0.76$ assuming a scan speed of 0.95 px/s and f_{dark} of $0.55Hz$. Alternatively, the predicted signal attenuation term near the dark current limit with a 6.8px/s scan speed is 0.16. Given these two factors, the detection limit for the slower 0.95px/s scan speed is predicted to be $\approx \frac{0.76}{0.16} = 4.76\times$ more sensitive than the detection limit at 6.8px/s. Dividing our limiting photon rate estimate of $6k$ph/s for the default bias setting, IMX-1, by this factor predicts a rate of $6/4.76 \approx 1.26k$ph/s at a the slower scan speed, consistent with the figure reported by Ralph et al. More importantly, given the analysis in Sec. 4.1, our best performing custom bias configuration was shown to outperform the default configuration by a factor of $2.6\times$, suggesting that with a slower scan speed and using the detection algorithm employed by Ralph et al. in [18], objects generating as few as $\frac{1.24k}{2.6} \approx 480$ph/s may be detectable.

Authors	Zolnowski et al. [19]	McMahon-Crabtree and Monet [10]	Ralph et al. [18]
EVS Model	Back-Side Illuminated (BSI) DAVIS	Gen-3*	Gen-4*
Aperture (mm)	90	60.7	200
Focal length (mm)	495	85	600
IFOV (arcsec/px)	7.71	48.5	1.67
Scan Rate (arcsec/s)	15.04	15.04	1.76
Scan Rate (px/s)	1.95	0.31	0.95
m_v limit	10.38	9.7	14.45
R_{ph} limit (kph/s)	10.7	9.1	**1.24**
*Prophesee			

Table 2 Summary of previous limiting magnitude estimates for EVS sensors. Reported optical system parameters are used to convert limiting magnitude to R_{ph} and scan rate from arcsec/s to px/s to directly compare results.

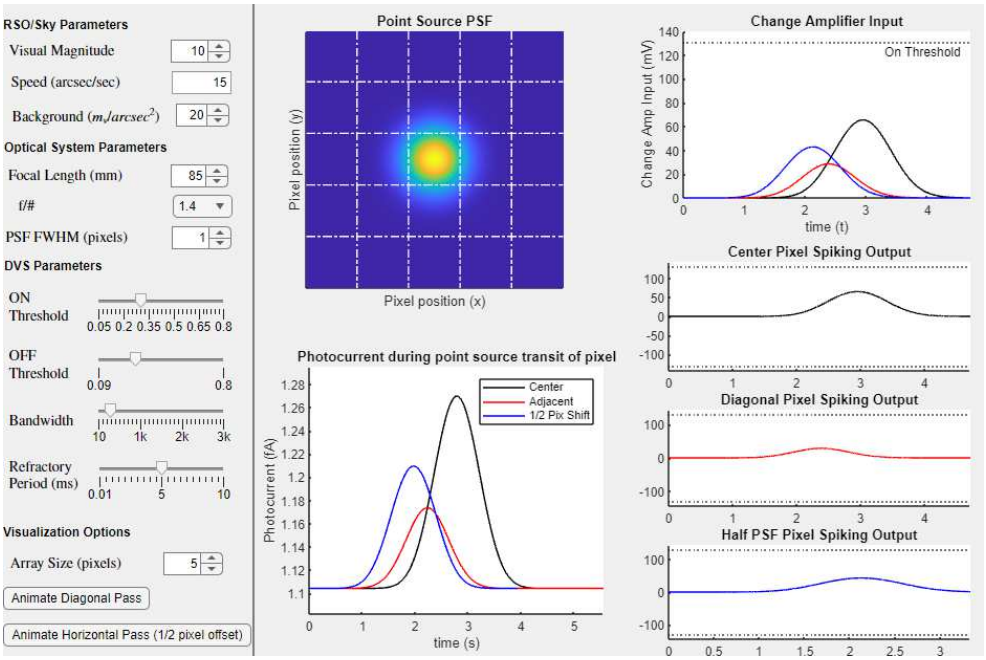


Fig. 8 EVS output simulation tool for SDA

5 EVS tool for SDA

Using the fit model parameters found in Sec. 4.3, we updated our open source EVS SDA tool with updated parameters to help design optical systems for exploiting

the IMX636 for detecting RSOs [2]. Figure 8 displays a screenshot of the GUI. User selectable parameters include visual magnitude of the object, speed (arcsec/sec), and sky brightness ($m_v/arcsec^2$). In addition, the tool allows the user to select optical system parameters including focal length, $f/\#$, and Point Spread Function (PSF) size (measured in pixels). ON/OFF thresholds can be tuned individually, in addition to bandwidth and refractory period; however, given the above analysis, for dimmer objects, bandwidth is limited by the photoreceptor so adjusting the slider bar in the application will not affect the temporal response of the simulation. A few options are also included for visualizing the response. The size of the PSF image in the top left can be adjusted, and the two types of simulated target trajectories can be animated. The diagonal pass simulates the target passing directly through the center of the pixel from one corner to the other, whereas the horizontal pass simulates the target passing parallel to one edge of the pixel with only half of the PSF infringing on the pixel of interest. This captures both the best-case and worst-case detection conditions: object passing through center with maximum transit time (best), and object transiting along the edge directly between two pixels (worst). The bottom left plot simulates photocurrent for both the center pixel and a diagonally adjacent pixel using a diagonal pass, as well as the horizontal pass with the object offset $\frac{1}{2}$ pixel width from center. The plots on the right simulate the continuous voltage input to the change amplifier and the spiking output of the comparators for each case.

Figure 9 illustrates how the tool predicts individual pixel response for several different cases of similar objects with different parameters. Part **a** shows how the diagonal pass produces a single ON and OFF event as the object transits the center pixel on a diagonal path, but no events for the diagonally offset pixel. **b** demonstrates how increasing the speed attenuates the pulse amplitude such that neither pixel generates an event, but part **c** shows how the same signal is detectable by reducing the thresholds. In this case, the thresholds are imbalanced to illustrate how a pixel can

[2] EVS-SDA Tool

respond with a different number of ON and OFF events depending on how the sensor is biased. Finally, part **d** shows how increasing the refractory period can also significantly influence pixel response by enforcing a longer wait time after each event before the comparator resumes tracking changes to the input signal.

6 Noise Analysis and Removal

In Sec. 4 we showed how our custom bias configuration can improve sensitivity by 2.6× or $1.05m_{\mathrm{V}}$ compared to default biases; however, this comes at the cost of increased noise rates. As a result, this noteworthy improvement in sensitivity is only effective for SDA if signal events can be reliably separated from noise events. Moreover, excessive noise rates diminish one of the key benefit of EVS, data sparsity. Figure 10 displays $\approx$ 45 seconds of on-sky recordings using the IMX636 sensor using **a** default biases and **b** our best-performing, custom bias configuration, IMX-6. These recordings were collected by Michal Zolnowski at his observatory near Krakow, Poland during the evening of 25 Jun, 2024 a Canon L-Series 200mm, f /2.8 lens. The mount was static such that sidereal motion caused the stars to streak across the Field of View (FOV), and for each recording, events were accumulated to generate the images. For each image, star streaks were manually observed and counted for comparison. As expected, the more sensitive bias configuration resulted in a higher number of visible streaks (54 compared to 32); however, the total number of events generated increased from a very modest $536k$ to over $132M$. A small portion of that increase can be attributed to the sensor generating larger number of signal events, but a majority of the increase is due to significantly higher noise rates.

Analyzing noise statistics, we applied two simple but effective strategies to combat the excess noise produced by our sensitive bias configuration as shown in Fig. 10. First, we removed "hot pixels". Hot pixels are a well known phenomenon that occurs in EVS that is caused by pixel to pixel threshold mismatch. A majority of pixels' threshold

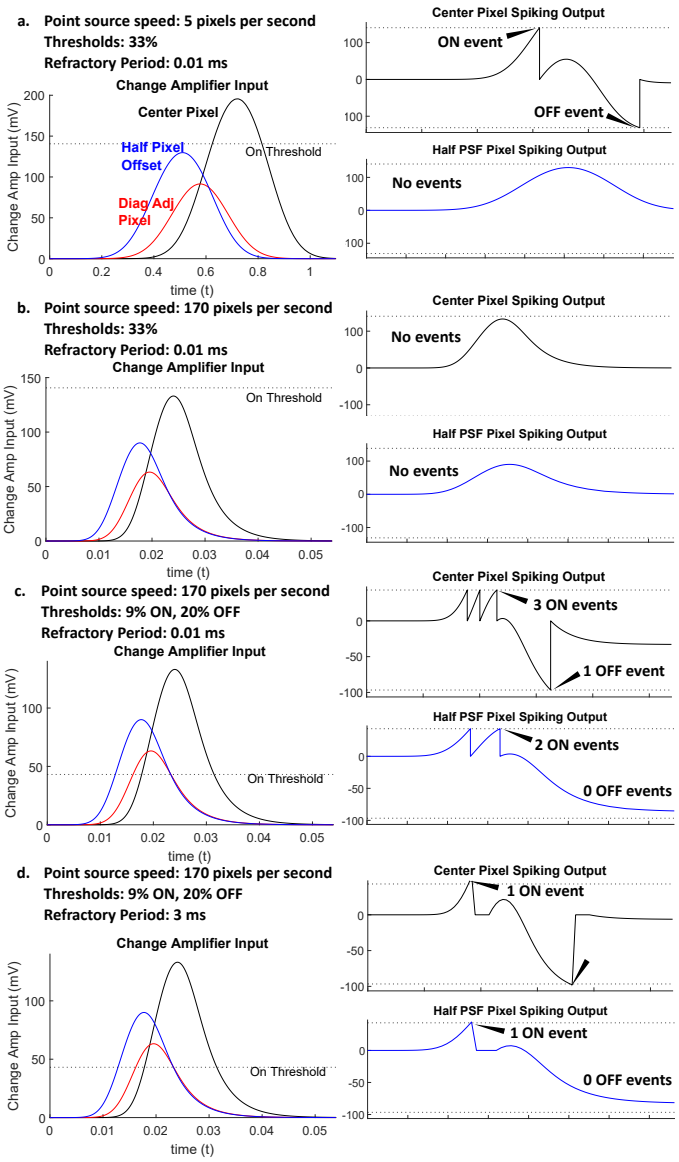


Fig. 9 Sample output of EVS-SDA tool demonstrating how different combinations of biases and speed affect sensor response to an object of identical brightness.

levels fall within a manageable tolerance of the nominal threshold level; however, in an array of $1M$ pixels, a small number will fall outside a few standard deviations in sensitivity. The most sensitive of these will fire at a near continuous, rapid rate

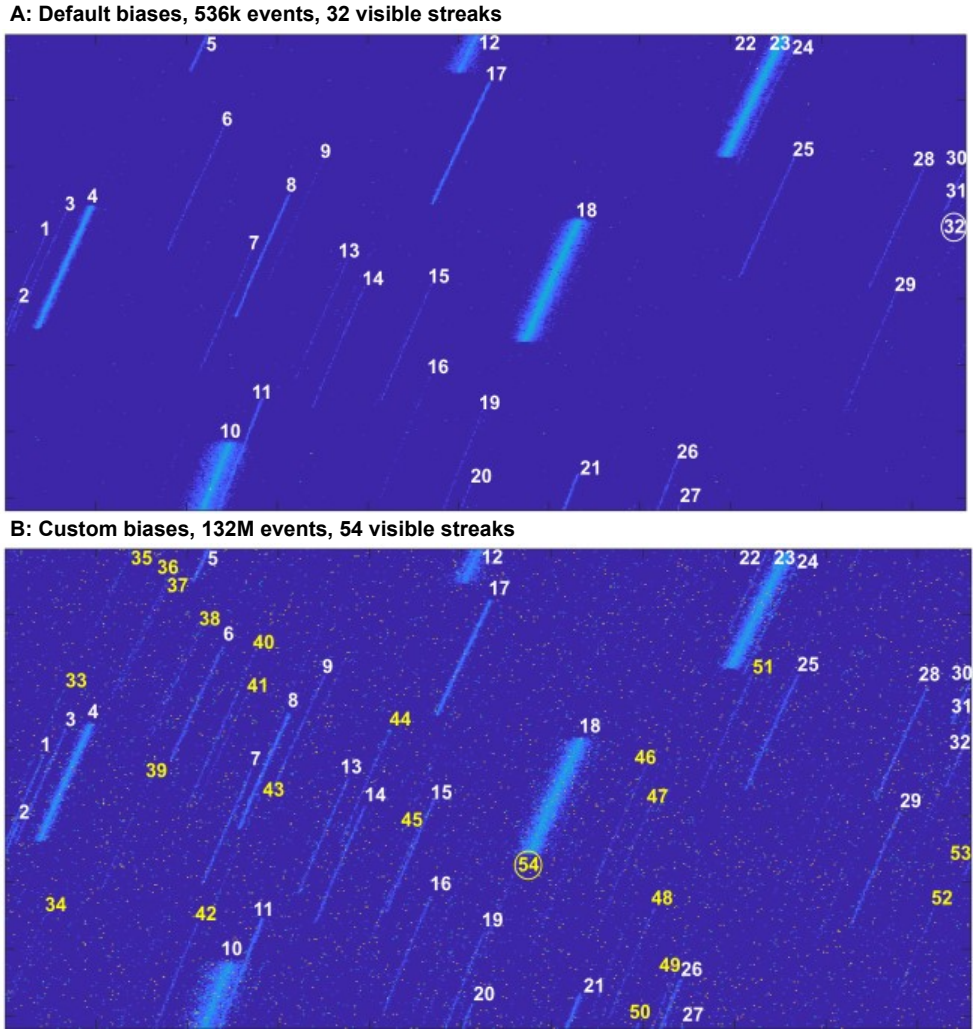


Fig. 10 Raw 45 second event accumulations from on-sky recordings using **A** Default, and **B** IMX-6 bias configurations.

due to shot noise on the input signal. Upon investigation, we found that over 99% of the excess events in our custom bias recording were caused by just 2% of the pixel array which we classified as hot pixels by setting a minimum cutoff value of ≈ 100 events per second. Figure 11 part A displays the same image from Fig. 10 **B** after hot pixel removal. Once hot pixels are removed the total data requirement is now only

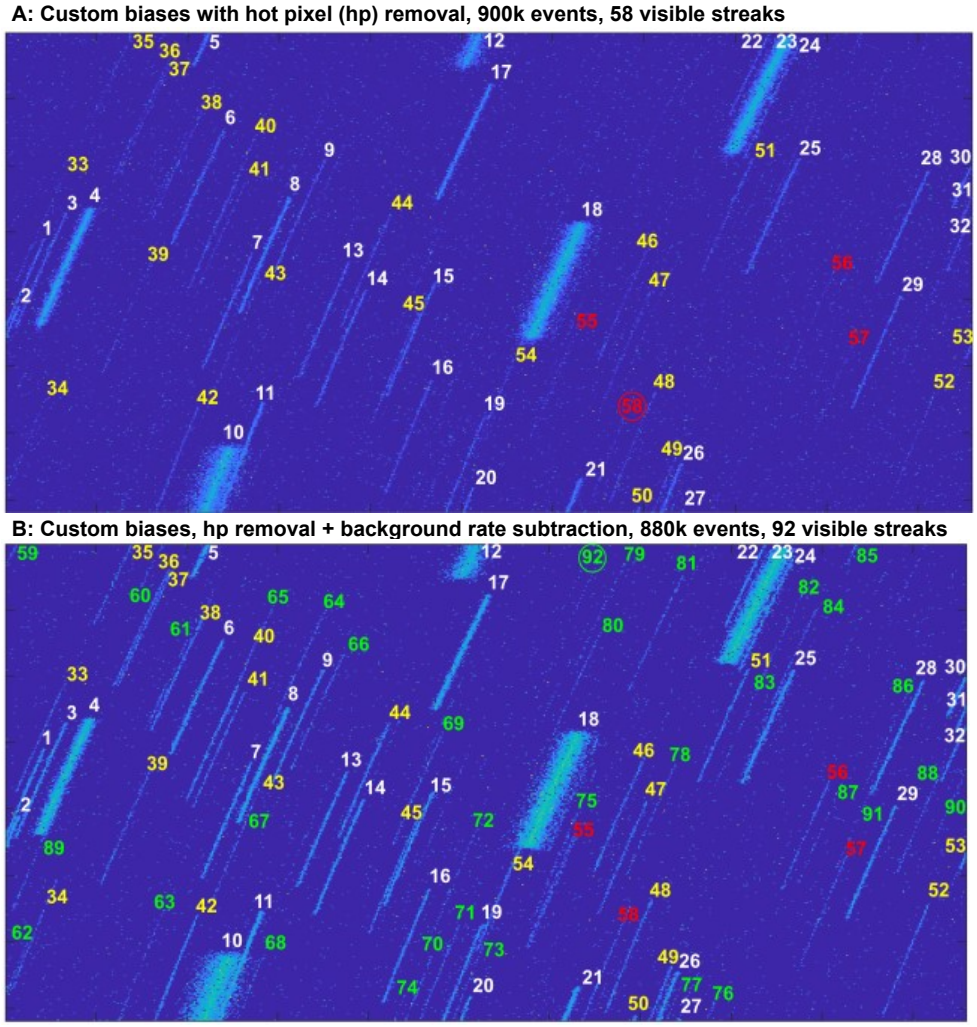


Fig. 11 Post-processed 45 second event accumulations from on-sky recordings using the IMX-6 bias configuration with **A** hot pixel removal only, and **B** both hot pixel removal and background rate subtraction.

67% higher than with default biases, and an additional four streaks are now visible, resulting in a total of 58.

Figure 11 **B** illustrates a second, novel denoising strategy that we developed in this study. While hot pixels are caused by a small fraction of pixels having abnormally low

threshold levels, in reality, each pixel has a slightly different threshold, and the distribution of threshold levels across the array is predominantly Gaussian. Furthermore, each polarity (ON and OFF) has a unique value for each pixel, meaning that the noise profile of each pixel is influenced by two threshold levels drawn independently from two Gaussian distributions with a mean value determined by a user-selectable bias and the standard deviation being the result of device mismatch, which is baked in to each pixel at fabrication. This means that even after hot pixel removal, some pixels still exhibit higher than average noise rates while others remain relatively quiet. Our proposed method exploits this understanding and assumes that each pixel's average noise rate will converge to a steady state value over a period of several seconds. Using the same bias configuration (IMX-6) we recorded pure noise with the lens cap on to simulate the night sky (both of which are assumed to be well below the dark current limit) for 15 seconds. For each pixel, we then found the average noise rate in pixels/second and subtracted each pixel's expected number of noise events during the 45 second recording from the recorded data. Figure 11 **b** shows the remarkable result that this simple method uncovers an additional 34 streaks for a total of 92! Combining our custom bias configuration with this simple denoising method increases the number of visible streaks by a factor of 2.9× with only a 64% increase in effective data rates. Notably, after denoising, the data rate is still extremely sparse at $19.5k$ events per second across the entire array, or ≈ 0.02 events per second per pixel. Both denoising methods are cheap computationally and could feasibly be performed prior to data downlink for orbital SDA applications, preserving advantageous data-sparsity of EVS output.

7 Photometric Mapping of EVS Response

The fit-model developed in Sec. 4 can be further leveraged to expand potential use cases of EVS by facilitating photometric reconstruction. Revisiting Fig. 2, the top plot

hints that low resolution photometric reconstruction of the input signal is theoretically possible from event output, provided the initial illumination level is known.

7.1 Key Model Parameters for Reconstruction

At the single pixel level the discretized nature of events implies that the uncertainty of this approach is on the order of the threshold, θ. Nonetheless, accurately characterizing the contrast thresholds is foundational to signal reconstruction. In the most simple model, assuming the sky background is well below the dark current limit, the number of ON events generated in a single pixel by an object producing I_{obj} photocurrent on the focal plane is proportional to the change in log-photocurrent divided by the ON threshold

$$N_{\text{on}} = \frac{1}{\theta_{\text{on}}} \left(\log \left(I_{\text{obj}} + I_{\text{dark}} \right) - \log \left(I_{\text{dark}} \right) \right) = \frac{1}{\theta_{\text{on}}} \log \left(\frac{I_{\text{obj}} + I_{\text{dark}}}{I_{\text{dark}}} \right). \tag{4}$$

Therefore, the two critical factors for reconstructing object brightness I_{obj} from ON events N_{on} are the pixel dark current I_{dark} and the ON threshold θ_{ON}.

In reality, there is an additional factor that complicates photometric reconstruction, particularly in the context of SDA. Even though EVS are known for their low-latency and high temporal resolution, their temporal response can be greatly reduced when the photocurrent is extremely low under dark conditions such as those inherent to nighttime SDA. This implies that a term describing the pixel's LPF attenuation is necessary to reconstruct photocurrent for objects moving at faster speeds. For sinusoidal signals passing through a first-order low-pass filter, signal attenuation is described by evaluating the magnitude of the transfer function

$$\left| \frac{V_{\text{out}}}{V_{\text{in}}} \right| = \frac{1}{\sqrt{\left(\frac{f}{f_{\text{cut}}} \right)^2 + 1}}, \tag{5}$$

where f_{cut} is the system's LPF corner frequency and f is the frequency of the sinusoidal input signal with amplitude V_{in}. V_{out}, therefore, is the amplitude of the output waveform. When the photocurrent is low, the photoreceptor itself acts as a LPF with a corner frequency that is directly proportional to the photocurrent[7]. As a result, defining a fixed f_{cut} is not suitable for reconstructing the brightness of very dim objects. To account for the illumination dependent LPF of the photoreceptor, we can define the corner frequency at the dark current limit f_{dark}, and use this value to determine the instantaneous corner frequency of the LPF transfer function as an object passes throught a pixel's FOV and momentarily increases the photocurrent on that pixel. Because the corner frequency depends monotonically on the current in the photodiode, the corner frequency is scaled by the same factor that appears in log term of Eq. (4),

$$f_{\text{cut}} = f_{\text{dark}} \frac{I_{\text{obj}} + I_{\text{dark}}}{I_{\text{dark}}}. \tag{6}$$

Finally, we assume that the photoreceptor circuit attenuates faster moving objects as a function of their speed. Although objects passing through a pixel's FOV do not produce a periodic signal, the photocurrent pulse of a focused point source does resemble a single period of a sine wave. Assuming the optical system's PSF is on the order of 1 pixel and the center of the object transits directly through the center of a pixel's FOV, the photocurrent begins to increase when the point source object is within 1/2 pixel-width of the target pixel, reaches a peak value when the object is centered on the target pixel, and decays to zero after it has moved another 1/2 pixel beyond. Therefore, the current pulse resembles one full period of a sine wave that is twice as wide spatially (or half as wide temporally) as a single pixel from trough to trough. Temporally then, a pixel transiting an objects at a speed of v_{pps} pixels per second will be attenuated similarly to a periodic signal with frequency $f = \frac{v_{\text{pps}}}{3.67}$. Piecing together these constraints, the expected number of ON events generated as a

dim object passes through a single pixel's FOV is predicted by

$$N_{\text{on}} = \frac{1}{\theta_{\text{on}}} \log(\Delta I) \frac{1}{\sqrt{\left(\frac{v_{\text{pps}}}{2 f_{\text{dark}} \Delta I}\right)^2 + 1}}, \tag{7}$$

where the ratio $\frac{I_{\text{obj}}+I_{\text{dark}}}{I_{\text{dark}}}$ is replaced by the term ΔI.

7.2 Background Illumination

Because EVS discard DC information, obtaining absolute photometric measurements has only recently been explored; however, since the night sky provides a uniform background illumination, we propose that EVS events can be used to directly measure point source brightness if the background illumination is estimated by another means (e.g. a Sky Quality Meter (SQM) measures sky brightness in magnitudes per arcsec^2 and can be purchased for a few $100). Alternatively, if the sky brightness is sufficiently below the dark current limit, no independent brightness estimate is required.

First, we confirmed the background illumination of our set-up to be well below the dark current limit. The ambient illuminance in the dark box was measured at $<$ 10mlux. If we assume the anodized surface has a reflectance of $\approx 10\%$, it is reasonable to assume the light reflected off the disk is Lambertian with illuminance $\leq$ 1mlux. Moreover, the conversion between scene illuminance and chip illuminance is given by

$$E_{\text{chip}} = E_{\text{scene}} \frac{1}{(4f/\#)^2}.^{3} \tag{8}$$

With our lens ($f/\# = 1.8$), the on-chip illuminance is only 1/13 the scene illuminance, so a very conservative estimate gives $E_{\text{chip}} = 0.1$mlx. To convert to photocurrent we can assume

$$I_{\text{ph}} = 1.12 \times 10^{16} E_{\text{chip}} \eta q p^2 \,, \tag{9}$$

[3] T. Delbruck, Notes on Practical Photometry

where η is average visual band Quantum Efficiency (QE), p is pixel pitch, 1.12×10^{16} the scalar conversion between lumens and visible-band photon flux from [17], and q the electron charge. Using this, we estimate the background photocurrent is $\approx$ 3aA, a few orders of magnitude below a reasonable dark current estimate for the IMX636 camera used in our study, $\approx 1fA$ [14].

7.3 Fitting the Response Model

Before applying the model predicted by Eq. (7) directly to measured response data, the factor of two that was proposed to relate v_{pps} to f_{cut} was further evaluated. A pixel's response due to a moving point source has a shape that resembles one full period of a sine wave with frequency $f = v_{\text{pps}}/2$, but it is not actually periodic. The MATLAB GUI described in [11][4] was used to simulate the attenuation of a photocurrent pulse generated by a moving point source of known illumination and using an intensity dependent LPF. Observing the simulated peak amplitude of the resulting current pulse for object speeds in the range of 0.1 to 1×10^3px/s, the half-power point was extracted to find the correct scaling term k between f and v_{pps}. Dividing the speed at which the half-power point was observed by the actual corner frequency applied in the simulation, we found $k = 3.67$.

Figure 12 shows that by properly adjusting the scaling term, the mathematical attenuation model better matches the simulated pixel response shown in blue. The simulated curve is shallower than the mathematical attenuation model in both cases because the illumination dependent corner frequency is updated instantaneously at each time step as the photocurrent increases. The attenuation model accounts for intensity dependent scaling of the corner frequency by calculating f_{cut} using the peak photocurrent (i.e. ΔI) observed during point source transit.

Our method of matching signal events in the most responsive pixels along each streak enabled testing the theoretical model developed in Sec. 7.1 to determine whether

[4] EVS SDA Tool

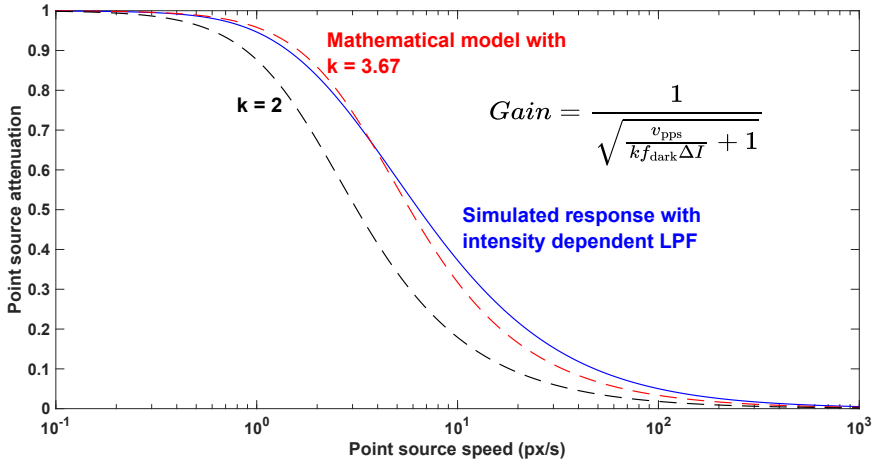


Fig. 12 Mathematical model for point source attenuation as a function of point source speed with scaling term k = 2 (black) and k = 3.67 (red). The blue curve is 'ground truth' obtained by simulating a moving Gaussian point source with PSF Full Width Half Max (FWHM) of 0.5 pixels and applying intensity dependent LPF.

accurate photometric reconstruction from events is feasible. Figure 7 plots the average matched ON events N_{on} per pixel (red circles) vs. object brightness in photons/s. We first analyzed the accuracy of the simplest model that disregards temporal response information and used Eq. (4) to fit the measured response and estimate parameters θ_{on} and I_{dark} using least squares regression. The black dashed curve in Fig. 7 shows the result of the simple model. The RMSE between the modeled and measured response (red circles) is $\approx$ 0.9 events/pixel, and the estimate clearly diverges significantly for dimmer point sources. Applying the model to a seven different bias configurations and examining the fit parameters, the average I_{dark} estimate is $\approx$ 5fA, several times higher than expected–and the θ_{on} estimates ranged from $\approx$ 0.02-0.06 log-contrast, which is significantly more sensitive than than reported values [3].

Previous analyses of temporal response have predicted that the cutoff frequency near the dark current limit is on the order of $\approx$ 1Hz, whereas our data points were collected with an object velocity of 6.8px/s. If the cutoff frequency was constant for all point sources, the fit model would not be affected; however, point sources of different

brightness levels individually adjust the cutoff frequency according to Eq. (6). As a result, we find the more sophisticated model proposed in Eq. (7) is required to capture the nuances of the EVS pixel response shown in Fig. 7. Pixel temporal response characteristics attenuate the signal of fast moving objects, and Eqs. (5) and (6) predict the degree of attenuation under dim conditions. In Eq. (7), we see that the term $\Delta I = \frac{I_{\text{src}}+I_{\text{dark}}}{I_{\text{dark}}}$ appears both in the log term and the LPF attenuation factor.

The blue curve of Fig. 7 shows the result of applying the updated fit model. Because most of the bias configurations we tested applied imbalanced ON and OFF thresholds, the term N_{offset} was also added to account for the fact that the background signal's reset is slightly higher than the mean value of the dark current prior to the first signal event. This occurs because the θ_{off} threshold is sufficiently large that noise rarely will generate an OFF event, and even if an OFF noise event occurs, it will be followed almost immediately by one or more ON events, causing the final reset level to be slightly elevated from the mean background (or dark current) value. Because the reset level is offset somewhat higher than the dark current (or background), the first few events are "missed". The complete fit model as illustrated in Fig. 7 is therefore

$$N_{\text{on}} = \frac{1}{\theta_{\text{on}}} \log\left(\Delta I\right) \frac{1}{\sqrt{\left(\frac{v_{\text{pps}}}{3.67 f_{\text{dark}} \Delta I}\right)^2 + 1}} - N_{\text{offset}}. \tag{10}$$

The blue curve qualitatively fits the data much better, and the updated model improves the RMSE to 0.15ev/px, a 6× improvement over the original fit. Across all seven bias configurations tested, fit parameter estimates for non-bias dependent terms were $I_{\text{dark}} = 1.1 \pm 0.5\text{fA}$, $f_{\text{dark}} = 0.55 \pm 0.2$ Hz. Parameters that vary with biases ranged between $0.05 < \theta_{\text{on}} < 0.15$ and $0.74 < N_{\text{offset}} < 1.02$ across the seven configurations. These estimates are more in line with those extrapolated from reported performance metrics in [3]. More importantly, we have demonstrated the ability to fit the average pixel response for moving point sources, unlocking an avenue for accurate

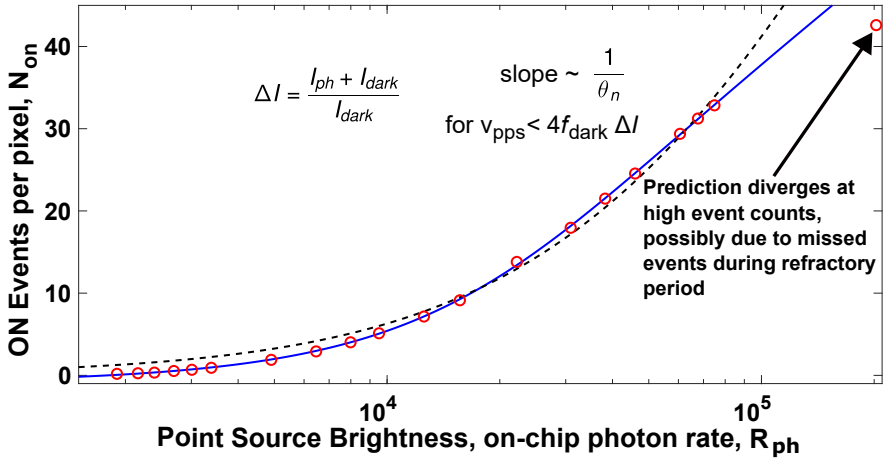


Fig. 13 Matched ON events vs. object brightness. The fit model described by Eq. (10) predicts that the slope of the curve converges to $1/\theta_{\text{on}}$ for the correct combination of object speed v_{pps} and object brightness I_{ph}.

photometric reconstruction from events, even when the objects are very dim, near the sensor's detection limit.

7.4 A Method for On-Sky Threshold Calibration

Figure 13 re-plots Fig. 7 with the y-axis (matched events) on a linear scale. The response appears to converge to a straight line when viewing brighter objects. Examining Eq. (10), the slope converges to $1/\theta_{\text{on}}$ when the cutoff frequency approaches a constant value. For instance, if

$$v_{\text{pps}} \leq 0.5 f_{\text{dark}} \Delta I, \tag{11}$$

the term representing the transfer function magnitude is ≥ 0.97, converging to 1 with increasing brightness.

This observation suggests a method for on-sky calibration of threshold levels if biases are dynamically tuned for different modes of operation between observations. By observing at least two different stars of known brightness at a sufficiently slow scan

speed to satisfy the inequality in Eq. (11), the result can be used to estimate θ_{on}. The average number of ON events observed in response to each object, N_1 and N_2, encodes to the log difference in illumination between the two. By assuming the scan speed is significantly slow such that the difference in LPF attenuation for both objects is negligible and writing equation Eq. (4) for both observations, we can subtract $N_2 - N_1$ to solve for θ_{on} and find

$$\theta_{\text{on}} = \frac{1}{N_2 - N_1} \log\left(\frac{I_2 + I_{\text{sky}} + I_{\text{dark}}}{I_1 + I_{\text{sky}} + I_{\text{dark}}}\right). \tag{12}$$

Again, I_{sky} can be ignored if $I_{\text{sky}} \ll I_{\text{dark}}$, but it is useful to translate sky brightness to transduced photocurrent in order to both predict when this inequality is satisfied and estimate limits when sky brightness is a factor. Sky brightness is typically reported in magnitudes per square arcsecond, and we already have the tools needed to compute photocurrent for the IMX636 pixel with a specific optical setup.

$$E_{\text{v}} = 10^{(-14.18 - m_{\text{v}})/2.5} \tag{13}$$

converts visual magnitude m_{v} to illuminance E_{v}, and

$$IFOV = \frac{p}{f} \times 206,265\,[\text{arcsec/radian}] \tag{14}$$

converts the pixel pitch p to Instantaneous Field-of-View (IFOV) in arcseconds. Multiplying sky brightness in $E_{\text{v}}/\text{arcsec}^2$ by the IFOV squared [arcsec^2], gives the illuminance caused by one pixel-sized patch of sky background at the entrance pupil. Equation (3) gives per-pixel photon rate as a function of illuminance at the entrance pupil. Finally, multiplying by quantum efficiency η and the elementary charge q, we estimate the photocurrent transduced per pixel for a given sky background. As an

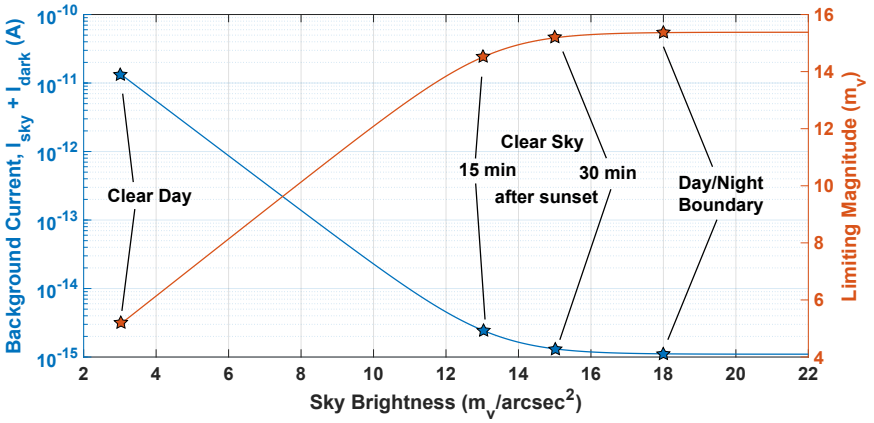


Fig. 14 Background current and predicted limiting magnitude for the IMX636 and optic used in [18] as a function of sky brightness. Model is based on IMX636 dark current and sensitivity estimated from fit model parameters.

example, a moonless clear night has a uniform brightness of $\approx 20 m_{\rm v}/\text{arcsec}^2$.[5] This means one square arcsecond of sky background produces 2.13×10^{-14}lx at the earth's surface. Assuming a 200mm aperture and 600mm focal length from [18], the IFOV is 1.67arcsec; therefore, the illuminance at the entrance pupil from a pixel-sized sky patch is $2.13 \times 10^{-14} \times 1.67^2 = 5.94 \times 10^{-14}$lx. All of the illuminance from the same pixel-sized patch of sky is then focused onto a single pixel on the focal plane. Therefore, the per pixel photon rate is 20.9ph/s, resulting in a background photocurrent $I_{\rm bg}$ of $\approx$ 2.2aA, a few orders of magnitude below the dark current of the IMX636 pixel.

Figure 14 plots the theoretical background photocurrent $I_{\rm bg} = I_{\rm sky} + I_{\rm dark}$ (blue) and predicted limiting magnitude $m_{\rm v}$ (orange) vs. sky brightness for the optical system used in [18]. We assume the IMX636 dark current is $I_{\rm dark} = 1.1$fA and $\theta_{\rm on} = 0.05$ from our fit model estimates described above, and the average visual band quantum efficiency is $\eta = 0.65$. Limiting magnitude is estimated by assuming the object must generate a sufficient photocurrent pulse to produce an ON event against the background level, or symbolically, $I_{\rm obj} > 0.05 \times (I_{\rm sky} + I_{\rm dark})$. Points corresponding to typical sky background measurement values under various conditions are marked.

[5] P. Schlyter, Radiometry and Photometry in Astronomy

McMahon-Crabtree and Monet created a similar plot based on empirical measurements and theoretical performance of the Gen-3 sensor with a much smaller lens, and used $18m_{\mathrm{v}}/\mathrm{arcsec}^2$ as the day-night boundary [10].

Assuming the bias configuration used for this study is viable with increased background illumination, this suggests the IMX636 and telescope from [18] with the bias configuration employed in our study could extend useful observation time with only a $0.87m_{\mathrm{v}}$ reduction from dark-sky sensitivity 15 minutes after sunset, and less than a 0.2 reduction after 30 minutes. However, it is possible that the sensitivity would need to be reduced (increased thresholds) due to changing noise properties with increasing background illumination [3, 9]. This theoretical limit extends $\approx 3m_{\mathrm{v}}/\mathrm{arcsec}^2$ below the day-night boundary used in [10] before an appreciable reduction in sensitivity. While observing satellites in full daylight with terrestrial observations is likely not possible, extending the time window for SDA observations by just 30 minutes into the early twilight hours is still a useful result. For some orbital applications, however, airglow from the atmosphere is less of a concern.

8 Conclusion

This paper explores the sensitivity limits of the most advanced EVS currently on the market, the Sony/Prophesee IMX636. Delving into the pixel circuit design, we developed and tested several custom bias configurations and showed that sensitivity for SDA can be improved by $1.05m_{\mathrm{V}}$. Additionally, we developed a model that allowed us to infer fundamental limitations of the sensor in terms of an on-chip, per-pixel photon rate, assuming focused, sub-pixel point source targets. We used these physical parameters to update our open source EVS SDA simulation tool to assist in designing optical systems that take advantage of EVS benefits to detect and track dim, sub-pixel RSOs. Finally, we developed a novel, simple yet remarkably effective denoising method to reduce the excess noise caused by our sensitive bias configuration, and demonstrated

the capability to detect 2.9× as many star streaks compared to default, stock sensor biases, while maintaining a sparse output data rate of just 0.02 events/second/pixel. These contributions clarify the capabilities of current EVS when pushed to the limit for SDA, and will hopefully fuel more widespread adoption in relevant applications.

In addition, this work facilitated a theoretical model for estimating the expected number of ON events generated by a point source of a particular brightness against a dark background, unlocking the potential for accurate photometric reconstruction with a EVS. Our analysis shows that by incorporating an illumination dependent LPF, we can fit the average pixel response to within a RMSE of 0.15 ev/pix along a "streak" generated as a point source transits across the IMX636 sensor's FOV. This model assumes the sky background is both uniform and well below the dark current limit of the sensor. The mathematical relationships needed to convert the sky brightness to fundamental units and thus extend our model to daytime SDA applications are also derived. Future work should include testing this model against on-sky recordings to further refine the model and analyze the effects of atmospheric turbulence. Ultimately, the improved modeling accuracy obtained through a deeper understanding of pixel operation and limitations has the potential to both improve the detection of dim objects and enable accurate photometric reconstruction of RSOs, extending the capabilities of EVS in SDA applications.

DISCLAIMER: The views expressed in this paper are those of the author and do not necessarily reflect the official policy or position of the United States Air Force Academy, the Air Force, the Department of Defense, or the U.S. Government.

[1] Gregory Cohen, Saeed Afshar, Brittany Morreale, Travis Bessell, Andrew Wabnitz, Mark Rutten, and André van Schaik. Event-based sensing for space situational awareness. *The Journal of the Astronautical Sciences*, 66(2):125–141, June 2019.

[2] T Delbruck and C A Mead. Adaptive photoreceptor with wide dynamic range. In *Proceedings of IEEE International Symposium on Circuits and Systems - ISCAS '94*, volume 4, pages 339–342 vol.4, May 1994.

[3] Thomas Finateu, Atsumi Niwa, Daniel Matolin, Koya Tsuchimoto, Andrea Mascheroni, Etienne Reynaud, Pooria Mostafalu, Frederick Brady, Ludovic Chotard, Florian LeGoff, Hirotsugu Takahashi, Hayato Wakabayashi, Yusuke Oike, and Christoph Posch. A 1280×720 back-illuminated stacked temporal contrast event-based vision sensor with 4.86µm pixels, 1.066GEPS readout, programmable event-rate controller and compressive data-formatting pipeline, 2020.

[4] Alex M Friedman and Carolin Frueh. Observability of light curve inversion for shape and feature determination exemplified by a case analysis. *The Journal of the Astronautical Sciences*, 69(2):537–569, April 2022.

[5] Guillermo Gallego, Tobi Delbruck, Garrick Orchard, Chiara Bartolozzi, Brian Taba, Andrea Censi, Stefan Leutenegger, Andrew J Davison, Jorg Conradt, Kostas Daniilidis, and Davide Scaramuzza. Event-based vision: A survey. *IEEE Trans. Pattern Anal. Mach. Intell.*, 44(1):154–180, January 2022.

[6] Rui Graca and Tobi Delbruck. Unraveling the paradox of intensity-dependent DVS pixel noise. *arXiv [eess.SY]*, September 2021.

[7] Yuhuang Hu, Shih-Chii Liu, and Tobi Delbruck. v2e: From video frames to realistic DVS events. In *Proceedings of the IEEE/CVF Conference on Computer Vision and Pattern Recognition*, pages 1312–1321, 2021.

[8] Patrick Lichtsteiner, Christoph Posch, and Tobi Delbruck. A 128×128 120 dB 15μs latency asynchronous temporal contrast vision sensor. *IEEE J. Solid-State Circuits*, 43(2):566–576, 2008.

[9] P N McMahon-Crabtree, L Kulesza, and others. Event-based camera refractory period characterization and initial clock drift evaluation. In *Unconventional*

Imaging, Sensing, and Adaptive Optics 2023. spiedigitallibrary.org, October 2023.

[10] Peter N McMahon-Crabtree and David G Monet. Commercial-off-the-shelf event-based cameras for space surveillance applications. *Appl. Opt., AO*, 60(25):G144–G153, September 2021.

[11] Brian McReynolds. *Benchmarking and pushing the boundaries of event camera performance for space and sky observations*. PhD thesis, 2024.

[12] Brian McReynolds, Rui Graca, and Tobi Delbruck. Exploiting alternating DVS shot noise event pair statistics to reduce background activity. In *2023 International Image Sensors Workshop (IISW)*, May 2023.

[13] Brian McReynolds, Rui Graca, R Oliver, M Nishiguchi, and Tobi Delbruck. Demystifying event-based sensor biasing to optimize signal to noise for space domain awareness. In *Advanced Maui Optical and Space Surveillance Technologies (AMOS)*, Advanced Maui Optical and Space Surveillance Technologies Conference (AMOS), September 2023.

[14] Brian J McReynolds, Rui Graca, Lucas Kulesza, and Peter McMahon-Crabtree. Re-interpreting the step-response probability curve to extract fundamental physical parameters of event-based vision sensors. In *Unconventional Optical Imaging IV*, volume 12996, pages 127–140. SPIE, June 2024.

[15] Brian J McReynolds, Rui Graca, Daniel O'Keefe, Rachel Oliver, Richard Balthazor, Nathaniel George, and Matthew McHarg. Modeling and decoding event-based sensor lightning response. In *Unconventional Imaging, Sensing, and Adaptive Optics 2023*, volume 12693, pages 335–352. SPIE, October 2023.

[16] Diederik Paul Moeys. *Analog and digital implementations of retinal processing for robot navigation systems*. PhD thesis, 2016.

[17] Russell J Palum. How many photons are there? *PICS*, pages 203–206, 2002.

[18] Nicholas Owen Ralph, Alexandre Marcireau, Saeed Afshar, Nicholas Tothill,

André van Schaik, and Gregory Cohen. Astrometric calibration and source characterisation of the latest generation neuromorphic event-based cameras for space imaging. *Astrodynamics*, 7(4):415–443, December 2023.

[19] Michał Żołnowski, Rafal Reszelewski, Diederik Paul Moeys, T Delbrück, and Krzysztof Kamiński. Observational evaluation of event cameras performance in optical space surveillance. In *NEO and Debris Detection Conference, Darmstadt, Germany*, 2019.